OPEN ACCESS
IOP Publishing
Superconductor Science and Technology
Supercond. Sci. Technol. 33 (2020) 025013 (8pp)
https://doi.org/10.1088/1361-6668/ab6179

Geometric scaling of two-level-system loss in superconducting resonators

David Niepce[1], **Jonathan J Burnett**[2], **Martí Gutierrez Latorre**[1] and **Jonas Bylander**[1]

[1] Chalmers University of Technology, Microtechnology and Nanoscience, SE-41296, Gothenburg, Sweden
[2] National Physical Laboratory, Hampton Road, Teddington, Middlesex, TW11 0LW, United Kingdom

E-mail: david.niepce@chalmers.se

Received 7 August 2019, revised 18 November 2019
Accepted for publication 13 December 2019
Published 8 January 2020

Abstract

We perform an experimental and numerical study of dielectric loss in superconducting microwave resonators at low temperature. Dielectric loss, due to two-level systems, is a limiting factor in several applications, e.g. superconducting qubits, Josephson parametric amplifiers, microwave kinetic-inductance detectors, and superconducting single-photon detectors. Our devices are made of disordered NbN, which, due to magnetic-field penetration, necessitates 3D finite-element simulation of the Maxwell–London equations at microwave frequencies to accurately model the current density and electric field distribution. From the field distribution, we compute the geometric filling factors of the lossy regions in our resonator structures and fit the experimental data to determine the intrinsic loss tangents of its interfaces and dielectrics. We put emphasis on the loss caused by a spin-on-glass resist such as hydrogen silsesquioxane (HSQ), used for ultrahigh lithographic resolution relevant to the fabrication of nanowires. We find that, when used, HSQ is the dominant source of loss, with a loss tangent of $\delta^{i}_{\mathrm{HSQ}} = 8 \times 10^{-3}$.

Keywords: disordered superconductor, two level systems, filling factor, participation ratio, microwave resonators, hydrogen silsesquioxane, 3D FEM simulation

(Some figures may appear in colour only in the online journal)

1. Introduction

Several modern circuits rely on superconducting devices with high microwave characteristic impedance and low dissipation. High impedance is usually implemented using the kinetic inductance of a chain of Josephson junctions [1–3] or with sub-micron-width wires made of a disordered superconductor such as NbN [4], NbTiN [5], or granular Al [6–8]. Despite being less studied, nanowires have some advantages over junction chains—high critical current, magnetic-field tolerance [5], strong coupling to zero-point fluctuations of the electric field [9, 10], less stringent constraints on device geometry, and absence of parasitic modes.

Applications of high-impedance devices include qubit architectures such as the fluxonium [3, 8], which depends on a superinductor (a low-loss inductor with reactive characteristic wave impedance exceeding the resistance quantum, $Z_c > R_Q \sim 6.5\,\mathrm{k\Omega}$ [1, 2, 4]) and travelling-wave microwave parametric amplifiers [11–17], relying on the kinetic inductance nonlinearity. Superconducting disordered nanowires are also interesting for newer types of microwave kinetic-inductance photon detectors [18, 19] and radio-frequency-readout of superconducting single-photon detectors [19, 20].

Dielectric loss and noise associated with two-level systems (TLS) residing in surfaces and interfaces are longstanding problems in superconducting circuits [21]. Specifically, TLS limit the quantum coherence times and lead to parameter fluctuations of superconducting qubits [22–25]. The participation ratios of the losses of the constituent dielectrics can be estimated through electro-magnetic simulation. Traditionally, the air-facing surfaces are found to be relatively insignificant,

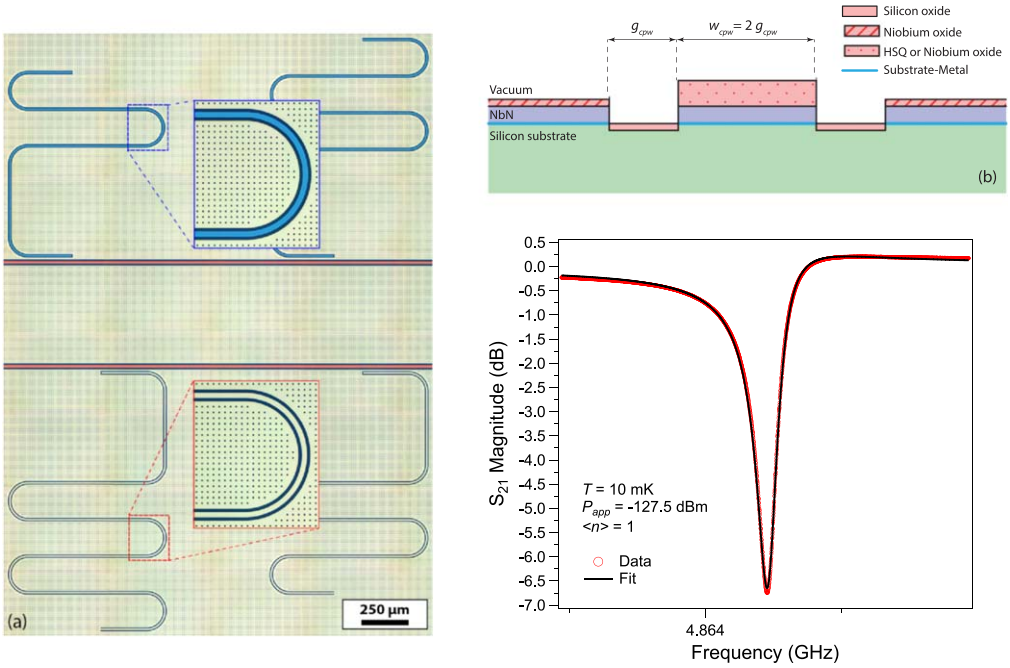

Figure 1. (a) False-coloured optical micrograph of the four resonators used in this work. The resonators are coupled to microwave feed lines (red overlay); the exposed Si substrate, where the NbN has been etched away, is in black. Additionally, HSQ covers the central conductor of the top resonators (cyan overlay). (b) Schematic of the cross-section of the resonators. (c) S_{21} magnitude response of a typical resonator in the single-photon regime (red points). The black line is a fit to determine the resonance parameters.

instead, the majority of the loss originates from the substrate-metal and substrate-air interfaces [26–30]. Moreover, for nanowires, the small dimensions exacerbate the TLS contribution to the loss, since the electric field becomes concentrated near the conductor edges. This concentration leads to an increase in the geometric filling factor (F) of the lossy dielectric layers compared to that of the loss-less vacuum. Therefore, it has been demonstrated that TLS remain the dominant loss mechanism even in disordered superconductors with high kinetic inductance, as long as the films are made moderately thin and not excessively disordered [4].

Across nanowire technologies it becomes necessary to use a spin-on-glass resist to define the sub-micron dimensions. The most prevalent spin-on-glass resist is hydrogen silsesquioxane, HSQ. While HSQ offers unmatched resolution ($\leqslant$10 nm [31]), its structure after development resembles porous amorphous silicon oxide [32, 33], which is a well-known host of TLS [34]. HSQ is hard to remove after e-beam exposure, and it is therefore often left on top of the finished devices [4].

Therefore, when attempting to understand and improve nanowire device performance, we have a rich landscape of small dimensions, disordered superconductors, and spin-on-glass dielectrics, all three of which are quite different from the more commonly used (and consequently well understood) wide ($>10\ \mu$m) Al or Nb features fabricated with conventional, removable resists.

In this paper, we explore the geometrical scaling, toward nanowire dimensions, of dielectric losses in microwave resonators. We make nominally identical devices with and without spin-on-glass top dielectric and clearly find that in all cases the HSQ makes microwave losses worse. Then, to quantify the loss contributions, we simulate the filling factors and find that due to the ratio of the device dimensions to the London penetration depth, disordered superconductors of small dimensions are not amenable to electrostatic simulations that are traditionally used. To accurately capture the physics, we instead perform 3D finite-element simulations of the current density and electric and magnetic fields at microwave frequencies, from which we extract the various filling factors. This reveals that, while the metal-air (MA) interface indeed has a small filling factor, the loss of the HSQ top dielectric is large enough to represent the largest combined loss, in agreement with measurements.

Combining measurements of the loss and numerical simulation of the filling factors of the different interfaces, we determine the value of the loss tangent of HSQ: $\delta^{i}_{\mathrm{HSQ}} = 8 \times 10^{-3}$, i.e. four times that of SiO_x [27, 29, 35], which would have been the assumption due to the similarities between spin-on-glass resists and silicon oxide.

2. Experimental methods, results

In order to study the geometric scaling of dielectric losses, we fabricated NbN coplanar waveguide resonators, with and without HSQ dielectric on top of the centre conductor. These devices span a range of widths of the centre conductor and of the gap between centre conductor and ground planes. The gap width ranges from $g_{cpw} = 500$ nm to 5 μm, with the ratio of the gap to the centre conductor kept fixed. Figure 1(a) shows a micrograph of a typical device, and figure 1(b) shows a sketch of the cross section of the resonators.

The samples are fabricated on a high-resistivity ($\rho \leqslant 10\,\mathrm{k}\Omega\,\mathrm{cm}$) (100) intrinsic silicon substrate. The substrate is dipped for 30 s in a 2% hydrofluoric acid (HF) bath to remove the silicon surface oxide. Within 5 min, the wafer is loaded into a UHV sputtering chamber, where a NbN thin-film of thickness 15 nm is deposited by reactive DC magnetron sputtering from a 99.99% pure Nb target in a 6:1 Ar:N_2 atmosphere at 12.7 μbar. Next, a 500 nm thick layer of PMMA A6 resist is spin-coated and then exposed by electron-beam lithography (EBL) to define the microwave circuitry and resonators. The pattern is developed for 60 s in MIBK: IPA (1:1) and transferred to the film by reactive ion etching in a 50:4 Ar:Cl_2 plasma at 50 W and 10 mTorr. In a subsequent EBL step, a 30 nm layer of HSQ is first spun and then exposed on the centre conductor of half of the microwave resonators such that, after development in a 2.45% TMAH solution, each sample has two copies of each design: one covered with HSQ and one without HSQ.

The samples are wire bonded in a connectorised copper sample box that is mounted onto the mixing chamber of a Bluefors LD250 dilution refrigerator. The inbound microwave signal is attenuated at each temperature stage by a total of 60 dB before reaching the device under test. Accounting for cable losses and sample-box insertion loss, the total attenuation of the signal reaching the sample is 70 dB. To avoid any parasitic reflections and noise leakage from amplifiers, the transmitted signal is fed through two microwave circulators (Raditek RADI-4.0-8.0-Cryo-4-77K-1WR) and a 4–8 GHz band pass filter. Finally, the signal is amplified by a LNF LNC4_8A HEMT cryogenic amplifier (45 dB gain) installed on the 2.8 K stage. Additional amplification is performed at room temperature (Pasternack PE-1522 gain-block amplifiers). This measurement environment has been shown to support measurements of resonators with quality factors of several millions [36] and therefore provides an ideal test bench for characterising loss in superconducting microwave resonators.

We study the microwave properties of each of these resonators by measuring the forward transmission (S_{21}) response using a Keysight N5249A vector network analyser. When probed with an applied power P_{app}, the average energy stored in a resonator of characteristic impedance Z_c and resonant frequency f_r is given by $\langle E_{int}\rangle = hf_r\langle n\rangle = Z_0 Q_l^2 P_{app}/\pi^2 Z_c Q_c f_r$, where $\langle n\rangle$ is the average number of photons in the resonator, h is Planck's constant, $Z_0 = 50\,\Omega$, and Q_c and Q_l are the coupling and loaded quality factors, respectively. Figure 1(c) shows a typical S_{21} magnitude response measured at 10 mK and has average photon population $\langle n\rangle = 1$. The resonator parameters are extracted by fitting the data with an open-source traceable fit routine [37].

In order to reliably determine the TLS loss contribution, we measure the resonant frequency of each resonator against temperature between 10 mK and 1 K [38, 39] using a Pound frequency-locked loop (P-FLL). We measured resonator pairs on the same chip, of the same length and gap widths, with/without HSQ on top of the centre conductor. The data is shown in figure 2, while the cryogenic microwave setup with the VNA and P-FLL schematics are explained in detail in [4]. This method only probes TLS effects and has the benefit of being sensitive to a wide frequency distribution of TLS. Consequently, the intrinsic loss tangent is robust against spectrally unstable TLS that produce time variations in the quality factor [40]. This allows us to independently determine the intrinsic loss tangent (times the filling factor) $F_{\mathrm{TLS}}\delta^i_{\mathrm{TLS}}$. The fitted values are presented in table 1.

3. Modelling of TLS loss

Figure 2 shows that in our devices, the losses are dominated by TLS, even for thin-film nanowires with widths down to 40 nm. In order to accurately account for the individual contributions of all TLS-containing regions of the circuit, we split the dielectric loss into a linear combination of loss tangents each associated with a corresponding filling factor [26–29, 41]

$$\frac{1}{Q_{\mathrm{TLS}}} = F_{\mathrm{TLS}}\delta^i_{\mathrm{TLS}} = \sum_k F_k \delta^i_k, \tag{1}$$

where δ^i_k is the intrinsic loss tangent of region k. Additionally, the filling factor of a given TLS host region k, of volume V_k and relative permittivity ε_k, is given by

$$F_k = \frac{U_k}{U_{total}} = \frac{\int_{V_k}\varepsilon_k \vec{E}^2(\vec{r})d\vec{r}}{\int_V \varepsilon \vec{E}^2(\vec{r})d\vec{r}}, \tag{2}$$

where U_k and U_{total} are the electric energy stored in region k and the total electric energy, respectively, $\vec{E}$ is the electric field, and ε is the effective permittivity of the entire volume V.

Several previous works have studied the loss participation of the different interfaces. O'Connell *et al* [35] perform low-temperature, low-power microwave measurements, report the intrinsic loss tangent of dielectrics, and interpret their results using a TLS defect model.

Wenner *et al* [26] numerically calculate the participation ratios of TLS losses in CPW and microstrip resonators, and find that the losses, at a level of $\delta \sim 5 \times 10^{-6}$, predominantly arise due to the substrate-metal (SM) and substrate-air (SA) interfaces, with only a 1% contribution from the MA interface.

Wang *et al* [27] conduct an experimental and numerical study of losses in Al transmon qubits and attribute the dominant loss to surface dielectrics, consistent with the TLS loss model. In a literature study of transmons made with the standard lift-off process, they find a seemingly universal value $\tan\delta \sim 2.6 \times 10^{-3}$. We note that the spread between data points pertaining to different devices is within the range of temporal variation, due to spectrally unstable TLS, recently reported in both qubit T_1 [25] and resonator Q [40].

Dial *et al* [28] experimentally study 3D transmon qubits, with results consistent with the SM and SA interfaces being the dominant contributors to loss.

Calusine *et al* [29, 30] trench the substrate of TiN resonators, achieving a mean low-power quality factor of

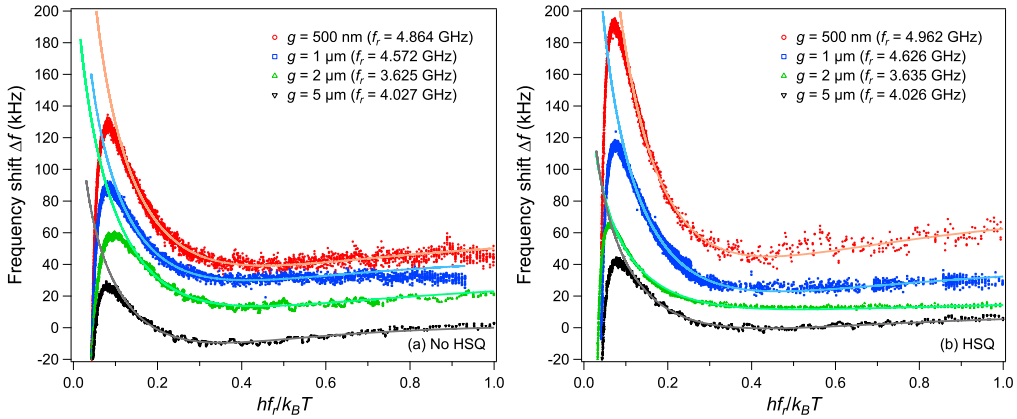

Figure 2. Frequency shift Δf as a function of the normalised frequency f_r of the measured resonators without HSQ (a) and with HSQ covering the central conductor (b). The data is obtained by applying $P_{app} = -110$ dBm and tracking the changes in resonant frequency against temperature between 10 mK and 1 K using the P-FLL. It is plotted against the natural energy scale of the TLS (hf_r/k_BT). The downturn in frequency occurring below $hf_r/k_BT = 0.1$ corresponds to the temperature-dependent kinetic inductance contribution and is not TLS-related. For clarity, the curves have been offset by 15 kHz. The solid lines are fits to $\Delta f(T) = F_{\mathrm{TLS}}\delta^i_{\mathrm{TLS}}(\ln(T/T_0) + [g(T, f_r) - g(T_0, f_r)])$ [38, 39], where $\Delta f(T) = [f_r(T) - f_r(T_0)]/f_r(T_0)$, T_0 is a reference temperature, $g(T, f) = \mathrm{Re}\left(\Psi\left(\frac{1}{2} + hf/2\pi ik_BT\right)\right)$, and Ψ is the complex digamma function.

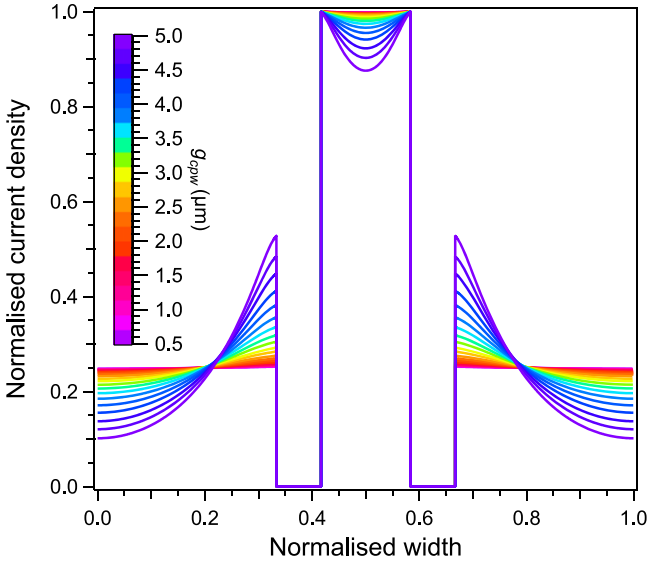

Figure 3. Simulated normalised current density inside the superconductors, extracted along a line half-way inside it (half the thickness), for all simulated values g_{cpw} in the 500 nm to 5 μm range.

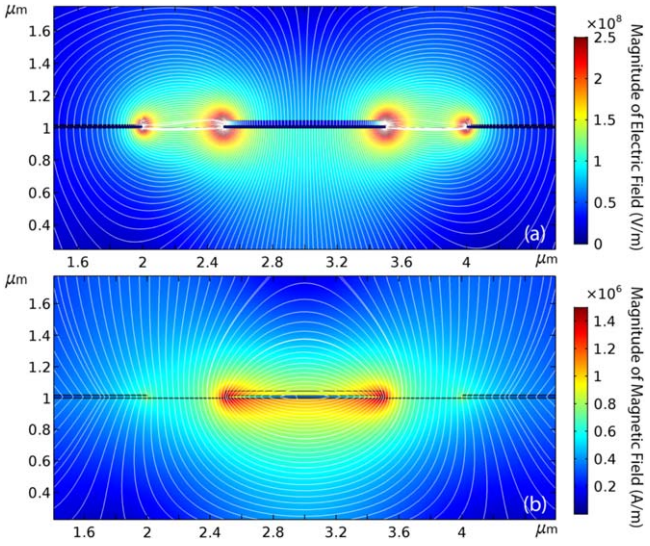

Figure 4. Magnitude and field lines of the simulated electric (a) and magnetic fields (b) for a cross section of the resonators with HSQ covering the central conductor. The permittivity in equation (5), with $\omega/2\pi = 5$ GHz, is given as an input to the Comsol Multiphysics simulation tool.

Table 1. Resonator parameters. $F_{\mathrm{TLS}}\delta^i_{\mathrm{TLS}}$ is obtained from fits of the data in figure 2.

g_{cpw} (μm)	Z_c (Ω)	f_r (no HSQ) (MHz)	f_r (with HSQ) (MHz)	$F_{\mathrm{TLS}}\delta^i_{\mathrm{TLS}}$ (no HSQ) ($\times 10^{-5}$)	$F_{\mathrm{TLS}}\delta^i_{\mathrm{TLS}}$ (with HSQ) ($\times 10^{-5}$)
5	207	4027	4026	1.36	1.66
2	312	3625	3635	1.60	1.87
1	441	4572	4626	1.98	2.50
0.5	632	4864	4962	2.74	3.92

3×10^6, and demonstrate agreement with a finite-element electrostatic simulation of dielectric loss.

4. Filling factor simulations

In order to analyse dielectric and interfacial losses in our devices, and in particular to identify those from the HSQ top dielectric, we perform electro-magnetic simulations (with and without the HSQ layer) in Comsol Multiphysics for a wide

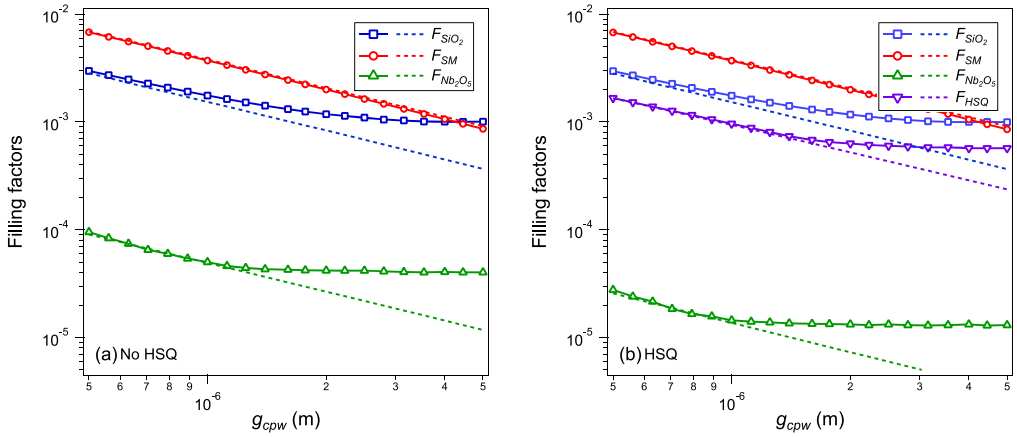

Figure 5. Simulated filling factors F as a function of the co-planar waveguide gap g_{cpw} for resonators without HSQ (a) and with HSQ covering the central conductor (b). The dashed lines represent the incorrect F obtained with electrostatic simulations.

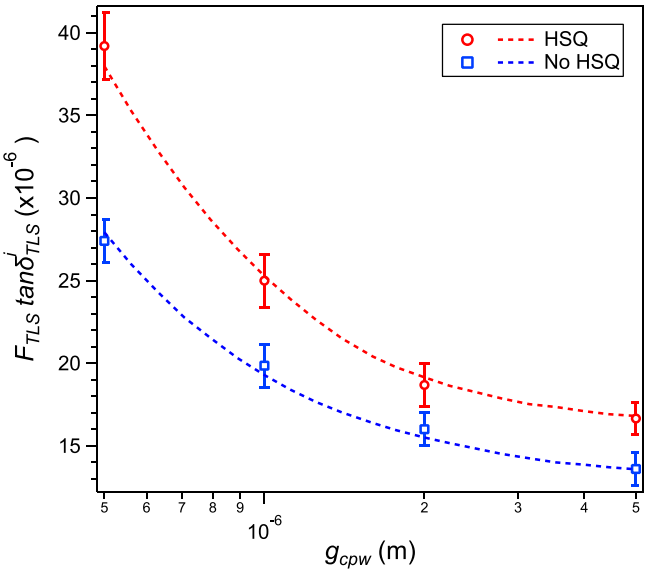

Figure 6. Total TLS loss $F_{\mathrm{TLS}}\delta^i_{\mathrm{TLS}}$ versus gap width g_{cpw} of the co-planar waveguide for all four measured resonators. The $F_{\mathrm{TLS}}\delta^i_{\mathrm{TLS}}$ values are determined from fits of the $\Delta f\,(T)$ data in figure 2—see table 1. The error bars represent two standard deviations of uncertainty (95% confidence interval). The dashed lines are fits to equation (1) using the simulated filling factors F_{TLS} shown in figure 5.

Table 2. Fitted loss tangents of the different lossy regions. The values are obtained from fits to equation (1) using the simulated filling factors.

Region	Symbol	Value
HSQ	δ^i_{HSQ}	8.0×10^{-3}
Substrate-metal interface	δ^i_{SM}	1.3×10^{-3}
Niobium oxide	$\delta^i_{\mathrm{Nb_2O_5}}$	4.7×10^{-2}
Silicon oxide	$\delta^i_{\mathrm{SiO_2}}$	2.1×10^{-3}

range of resonator geometries. A sketch of the cross-section of the simulated structures is shown in figure 1(b). The simulation parameters for the constituent materials are as follows: the SA interface is modelled as a 5 nm thick layer of SiO_2 [42] with relative permittivity $\varepsilon_r(SiO_2) = 4.2$. The MA interface consists of a 5 nm thick layer of Nb_2O_5 [43] with relative permittivity $\varepsilon_r(Nb_2O_5) = 33$ [44, 45]. The SM interface is modelled by a 2 nm thick layer inside the substrate ($\varepsilon_r(\mathrm{SM}) = \varepsilon_r(\mathrm{Si}) = 11.7$) [29]. Finally, the HSQ region has a thickness of 30 nm and relative permittivity $\varepsilon_r(\mathrm{HSQ}) = 3$ [33]. Because Nb_2O_5 requires several days to achieve any meaningful thickness [43], it is assumed that no Nb_2O_5 is present underneath the HSQ. Therefore, on the samples without HSQ, Nb_2O_5 resides on both the central conductor and ground planes, whereas on the samples with HSQ, Nb_2O_5 is present only on the ground planes.

The superconductor part of the structure requires extra care to simulate accurately: strongly disordered superconductors, like NbN, have an extremely small electron mean free path l (on the order of 0.5 nm and smaller [46]) and are therefore in the local dirty limit [47]. In this limit, several quantities become dependent on the mean free path and need to be adjusted from their BCS values [48, 49]. Most importantly for this study, the magnetic penetration depth in disordered superconductors and at zero temperature becomes

$$\lambda_{dirty}(0) = \lambda_L(0)\sqrt{\frac{\xi_0}{l}} = \sqrt{\frac{\hbar}{\pi\mu_0\Delta_0\sigma_n}}, \tag{3}$$

where $\lambda_L(0)$ is the London penetration depth at $T = 0$ K, ξ_0 is the BCS coherence length, $\hbar$ is the reduced Planck constant, μ_0 is the vacuum permeability, Δ_0 is the superconducting gap at zero temperature, and σ_n is the normal-state conductivity. Additionally, the temperature dependence of the penetration depth is given by

$$\frac{\lambda_{dirty}(T)}{\lambda_{dirty}(0)} = \left[\frac{\Delta(T)}{\Delta_0}\tanh\left(\frac{\Delta(T)}{2k_BT}\right)\right]^{-1/3}. \tag{4}$$

By measuring the resistance versus temperature of our NbN thin films, we find $T_c = 7.20$ K and $\sigma_n = 1.32 \times 10^5$ S m^{-1} (measured at the onset of the superconducting transition). Using $\Delta_0 = 2.08k_BT_c$ [50], we obtain $\lambda_{dirty} = 987$ nm $\simeq 1$ μm, which is comparable to the lateral dimension of our resonators.

Consequently, it is not sufficient to approximate the current density in our NbN devices as a surface density, since magnetic fields significantly penetrate the superconductor.

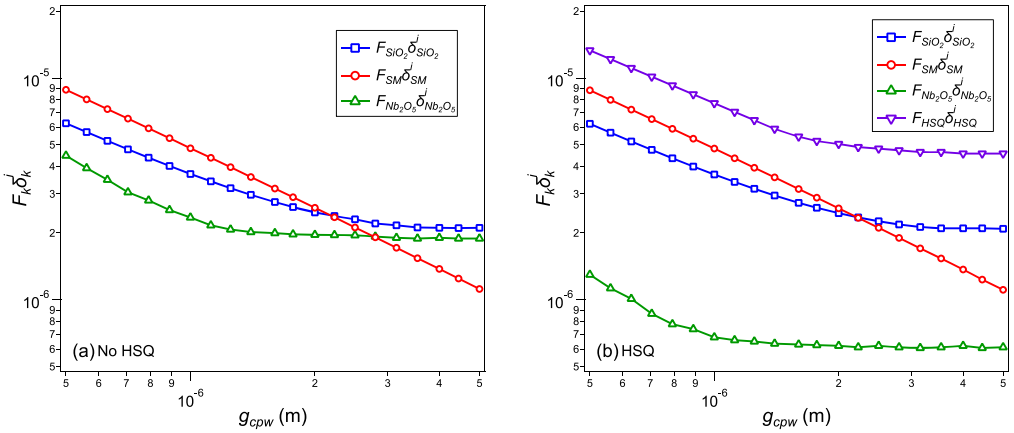

Figure 7. Contribution of each individual lossy region for resonators without HSQ (a) and with HSQ (b) covering the central conductor.

This is in contrast to resonators made of a conventional superconductor such as aluminium ($\lambda_L(0) \simeq 30$ nm [51]) or niobium (100 nm [52]). In a similar way, it is insufficient to assume a uniform current distribution in the superconductor when the resonator dimensions are larger than $\lambda_L(T)$.

Therefore, a static solution of Maxwell's equations is insufficient here, in particular for the wider geometries. Instead we need to solve the Maxwell–London equations, at the relevant frequency of the alternating current, in order to accurately simulate the densities of the current and electromagnetic fields. We achieve this in a 3D finite-element simulator by considering the superconductor as an environment with a complex permittivity [53, 54]

$$\varepsilon_r(\omega, T) = \varepsilon_0 - \frac{1}{\omega^2 \mu_0 \lambda_{dirty}(T)^2} - j\frac{\sigma_1(\omega, T)}{\omega}, \qquad (5)$$

where $\sigma_1(\omega, T)$ is the real part of the Mattis–Bardeen conductivity.

The meshing of the simulated structure has to be carefully optimised due the vast difference of length scales within the resonator structure (widths, thicknesses, and also the wavelength). The simulation mesh is manually defined using Comsol's swept mesh functionality and consists of rectangular elements. Rectangular elements are preferred over the more standard tetrahedral elements to avoid poor meshing quality inherent to high-aspect ratio tetrahedrons. The edge length of each element is varied from 3 nm to 100 nm, with smaller elements close to the regions of interest (superconducting thin-film and dielectric layers). Due to memory constraints, however, the edge length alongside the wave propagation direction is kept constant to 100 nm and only a short section of co-planar waveguide is simulated ($l_{cpw} = 4\ \mu$m). A relative tolerance of 1×10^{-5} was found as a good compromise between the accuracy of the converged solution and the duration of the simulation.

Figures 3 and 4 show the simulated current density and electric and magnetic fields, respectively, for a cross section of a resonator with $g_{cpw} = 500$ nm. From the electric fields, we calculate the filling factor of each region using equation (2) and present the result in figure 5. Additionally, figure 5 shows filling factors calculated by means of electrostatic simulation to highlight the significant deviation from the Maxwell–London simulation results for $w_{cpw} > \lambda_L$.

Using these simulated filling factors, we can fit equation (1) to the experimental results in table 1—see figure 6—and in this way determine the intrinsic loss tangent of each lossy region. These results are summarised in table 2.

5. Discussion

Our results are consistent with values found by other groups in similar types of devices [27, 29, 35, 44]. However, we emphasise that the fabrication of our devices was not focused on minimising the influence of TLS.

We find the intrinsic loss tangent for HSQ to be $\delta^i_{\mathrm{HSQ}} = 8.0 \times 10^{-3}$. Paired with the relatively large filling factor of the HSQ region, this makes HSQ the dominant contribution to the loss for all dimensions, as highlighted in figure 7; and for a given dimension, $F_{\mathrm{TLS}}\delta^i_{\mathrm{TLS}}$ is systematically higher for the sample covered with HSQ, as shown in figure 6. These results confirms that the porous amorphous silicon oxide structure of developed HSQ [32, 33] is a major source of dielectric loss, and therefore, a process that allows for the removal of the HSQ mask would lead to significant improvements in device performance.

6. Conclusion

In conclusion, we fabricated and measured co-planar waveguide resonators with dimensions ranging from $g_{cpw} = 5\ \mu$m down to 500 nm in order to study the geometric dependence of TLS loss. Using 3D finite-element electro-magnetic simulations we calculated the relative contributions of the different sources of TLS loss. Such simulations provide a valuable tool to predict the performance of superconducting resonators and other superconducting quantum devices.

Additionally, by comparing resonators with the central conductor covered by HSQ and resonators without HSQ, we were able to extract the intrinsic loss tangent of this dielectric: $\delta^i_{\mathrm{HSQ}} = 8.0 \times 10^{-3}$.

Acknowledgments

We acknowledge support in the device fabrication from the Chalmers Nanofabrication Laboratory staff. The authors are grateful to Philippe Tassin for granting access to his nodes in the Chalmers C3SE computational cluster where our simulations were performed. This research has been supported by funding from the Swedish Research Council and Chalmers Area of Advance Nanotechnology. In addition, JJB acknowledges financial support from the Industrial Strategy Challenge Fund Metrology Fellowship as part of the UK government's Department for Business, Energy and Industrial Strategy.

ORCID iDs

David Niepce https://orcid.org/0000-0002-3864-0658
Martí Gutierrez Latorre https://orcid.org/0000-0001-6041-3139

References

[1] Masluk N A, Pop I M, Kamal A, Minev Z K and Devoret M H 2012 Microwave characterization of josephson junction arrays: implementing a low loss superinductance *Phys. Rev. Lett.* **109** 137002
[2] Bell M T, Sadovskyy I A, Ioffe L B, Kitaev A Y and Gershenson M E 2012 Quantum superinductor with tunable nonlinearity *Phys. Rev. Lett.* **109** 137003
[3] Vladimir E, Manucharyan Jens, Koch Leonid I, Glazman and Devoret Michel H 2009 Fluxonium: single cooper-pair circuit free of charge offsets *Science* **326** 113–6
[4] Niepce D, Burnett J and Bylander J 2019 High kinetic inductance NbN nanowire superinductors *Phys. Rev. Appl.* **11** 044014
[5] Samkharadze N, Bruno A, Scarlino P, Zheng G, DiVincenzo D P, DiCarlo L and Vandersypen L M K 2016 High-kinetic-inductance superconducting nanowire resonators for circuit QED in a magnetic field *Phys. Rev. Appl.* **5** 044004
[6] Rotzinger H, Skacel S T, Pfirrmann M, Voss J N, Münzberg J, Probst S, Bushev P, Weides M P, Ustinov A V and Mooij J E 2016 Aluminium-oxide wires for superconducting high kinetic inductance circuits *Supercond. Sci. Technol.* **30** 025002
[7] Zhang W, Kalashnikov K, Lu W-S, Kamenov P, DiNapoli T and Gershenson M E 2019 Microresonators fabricated from high-kinetic-inductance aluminum films *Phys. Rev. Appl.* **11** 011003
[8] Grünhaupt L *et al* 2019 Granular aluminium as a superconducting material for high-impedance quantum circuits *Nat. Mater.* **18** 816–9
[9] Stockklauser A, Scarlino P, Koski J V, Gasparinetti S, Andersen C K, Reichl C, Wegscheider W, Ihn T, Ensslin K and Wallraff A 2017 Strong coupling cavity QED with gate-defined double quantum dots enabled by a high impedance resonator *Phys. Rev.* X **7** 011030
[10] Samkharadze N, Zheng G, Kalhor N, Brousse D, Sammak A, Mendes U C, Blais A, Scappucci G and Vandersypen L M K 2018 Strong spin-photon coupling in silicon *Science* **359** 1123–7
[11] Eom B H, Day P K, LeDuc H G and Zmuidzinas J 2012 A wideband, low-noise superconducting amplifier with high dynamic range *Nat. Phys.* **8** 623
[12] Bockstiegel C, Gao J, Vissers M R, Sandberg M, Chaudhuri S, Sanders A, Vale L R, Irwin K D and Pappas D P 2014 Development of a broadband NbTiN traveling wave parametric amplifier for MKID readout *J. Low Temp. Phys.* **176** 476–82
[13] O'Brien K, Macklin C, Siddiqi I and Zhang X 2014 Resonant phase matching of josephson junction traveling wave parametric amplifiers *Phys. Rev. Lett.* **113** 157001
[14] White T C *et al* 2015 Traveling wave parametric amplifier with Josephson junctions using minimal resonator phase matching *Appl. Phys. Lett.* **106** 242601
[15] Macklin C, O'Brien K, Hover D, Schwartz M E, Bolkhovsky V, Zhang X, Oliver W D and Siddiqi I 2015 A near-quantum-limited Josephson traveling-wave parametric amplifier *Science* **350** 307–10
[16] Vissers M R, Erickson R P, Ku H-S, Vale L, Wu X, Hilton G C and Pappas D P 2016 Low-noise kinetic inductance traveling-wave amplifier using three-wave mixing *Appl. Phys. Lett.* **108** 012601
[17] Adamyan A A, de Graaf S E, Kubatkin S E and Danilov A V 2016 Superconducting microwave parametric amplifier based on a quasi-fractal slow propagation line *J. Appl. Phys.* **119** 083901
[18] Janssen R M J, Endo A, Baselmans J J A, de Visser P J, Barends R and Klapwijk T M 2012 Power handling and responsivity of submicron wide superconducting coplanar waveguide resonators *J. Low Temp. Phys.* **167** 354–9
[19] Schroeder E, Mauskopf P, Mani H, Bryan S, Berggren K K and Zhu D 2019 Operation of a superconducting nanowire in two detection modes: KID and SPD *J. Low Temp. Phys.* **194** 386–93
[20] Sinclair A K, Schroeder E, Zhu D, Colangelo M, Glasby J, Mauskopf P D, Mani H and Berggren K K 2019 Demonstration of microwave multiplexed readout of DC-Biased superconducting nanowire detectors *IEEE Trans. Appl. Supercond.* **29** 1–4
[21] Müller Clemens, Cole Jared H and Lisenfeld Jürgen 2019 Towards understanding two-level-systems in amorphous solids: insights from quantum circuits *Reports on Progress in Physics* **82** 124501
[22] Müller C, Lisenfeld J, Shnirman A and Poletto S 2015 Interacting two-level defects as sources of fluctuating high-frequency noise in superconducting circuits *Phys. Rev.* B **92** 035442
[23] Klimov P V *et al* 2018 Fluctuations of energy-relaxation times in superconducting qubits *Phys. Rev. Lett.* **121** 090502
[24] Schlör S, Lisenfeld J, Müller C, Bilmes A, Schneider A, Pappas D P, Ustinov A V and Weides M 2019 Correlating decoherence in transmon qubits: low frequency noise by single fluctuators *Phys. Rev. Lett.* **123** 190502
[25] Burnett J J, Bengtsson A, Scigliuzzo M, Niepce D, Kudra M, Delsing P and Bylander J 2019 Decoherence benchmarking of superconducting qubits *NPJ Quantum Inf.* **5** 54
[26] Wenner J *et al* 2011 Surface loss simulations of superconducting coplanar waveguide resonators *Appl. Phys. Lett.* **99** 113513
[27] Wang C, Axline C, Gao Y Y, Brecht T, Chu Y, Frunzio L, Devoret M H and Schoelkopf R J 2015 Surface participation and dielectric loss in superconducting qubits *Appl. Phys. Lett.* **107** 162601
[28] Dial O, McClure D T, Poletto S, Keefe G A, Rothwell M B, Gambetta J M, Abraham D W, Chow J M and Steffen M 2016 Bulk and surface loss in superconducting transmon qubits *Supercond. Sci. Technol.* **29** 044001

[29] Calusine G *et al* 2018 Analysis and mitigation of interface losses in trenched superconducting coplanar waveguide resonators *Appl. Phys. Lett.* **112** 062601
[30] Woods W, Calusine G, Melville A, Sevi A, Golden E, Kim D K, Rosenberg D, Yoder J L and Oliver W D 2019 Determining interface dielectric losses in superconducting coplanar-waveguide resonators *Phys. Rev. Appl.* **12** 014012
[31] Chen Y, Yang H and Cui Z 2006 Effects of developing conditions on the contrast and sensitivity of hydrogen silsesquioxane *Microelectron. Eng.* **83** 1119–23
[32] Namatsu H, Yamaguchi T, Nagase M, Yamazaki K and Kurihara K 1998 Nano-patterning of a hydrogen silsesquioxane resist with reduced linewidth fluctuations *Microelectron. Eng.* **41–42** 331–4
[33] Liu P T *et al* 1998 The effects of plasma treatment for low dielectric constant hydrogen silsesquioxane (HSQ) *Thin Solid Films* **332** 345–50
[34] Barends R, Hortensius H L, Zijlstra T, Baselmans J J A, Yates S J C, Gao J R and Klapwijk T M 2008 Contribution of dielectrics to frequency and noise of NbTiN superconducting resonators *Appl. Phys. Lett.* **92** 223502
[35] O'Connell A D *et al* 2008 Microwave dielectric loss at single photon energies and millikelvin temperatures *Appl. Phys. Lett.* **92** 112903
[36] Burnett J, Bengtsson A, Niepce D and Bylander J 2018 Noise and loss of superconducting aluminium resonators at single photon energies *J. Phys.: Conf. Ser.* **969** 012131
[37] Probst S, Song F B, Bushev P A, Ustinov A V and Weides M 2015 Efficient and robust analysis of complex scattering data under noise in microwave resonators *Rev. Sci. Instrum.* **86** 024706
[38] Gao J, Daal M, Vayonakis A, Kumar S, Zmuidzinas J, Sadoulet B, Mazin B A, Day P K and Leduc H G 2008 Experimental evidence for a surface distribution of two-level systems in superconducting lithographed microwave resonators *Appl. Phys. Lett.* **92** 152505
[39] Lindström T, Healey J E, Colclough M S, Muirhead C M and Tzalenchuk A Y 2009 Properties of superconducting planar resonators at millikelvin temperatures *Phys. Rev.* B **80** 132501
[40] Earnest C T, Béjanin J H, McConkey T G, Peters E A, Korinek A, Yuan H and Mariantoni M 2018 Substrate surface engineering for high-quality silicon/aluminum superconducting resonators *Supercond. Sci. Technol.* **31** 125013
[41] Gambetta J M, Murray C E, Fung Y-K-K, McClure D T, Dial O, Shanks W, Sleight J W and Steffen M 2017 Investigating surface loss effects in superconducting transmon qubits *IEEE Trans. Appl. Supercond.* **27** 1–5
[42] Morita M, Ohmi T, Hasegawa E, Kawakami M and Ohwada M 1990 Growth of native oxide on a silicon surface *J. Appl. Phys.* **68** 1272–81
[43] Henry M D, Wolfley S, Young T, Monson T, Pearce C J, Lewis R, Clark B, Brunke L and Missert N 2017 Degradation of superconducting Nb/NbN films by atmospheric oxidation *IEEE Trans. Appl. Supercond.* **27** 1–5
[44] Kaiser C, Skacel S T, Wünsch S, Dolata R, Mackrodt B, Zorin A and Siegel M 2010 Measurement of dielectric losses in amorphous thin films at gigahertz frequencies using superconducting resonators *Supercond. Sci. Technol.* **23** 075008
[45] Romanenko A and Schuster D I 2017 Understanding quality factor degradation in superconducting niobium cavities at low microwave field amplitudes *Phys. Rev. Lett.* **119** 264801
[46] Chockalingam S P, Chand M, Jesudasan J, Tripathi V and Raychaudhuri P 2008 Superconducting properties and Hall effect of epitaxial NbN thin films *Phys. Rev.* B **77** 214503
[47] Dressel M 2013 Electrodynamics of metallic superconductors *Adv. Condens. Matter Phys.* **2013** 104379
[48] Gor'kov L P 1959 Microscopic derivation of the Ginzburg–Landau equations in the theory of superconductivity *J. Exp. Theor. Phys.* **9** 1364
[49] Tinkham M 2004 *Introduction to Superconductivity* (New York: Dover)
[50] Mondal M, Kamlapure A, Chand M, Saraswat G, Kumar S, Jesudasan J, Benfatto L, Tripathi V and Raychaudhuri P 2011 Phase fluctuations in a strongly disordered s-Wave NbN superconductor close to the metal-insulator transition *Phys. Rev. Lett.* **106** 047001
[51] Maloney M D, de la Cruz F and Cardona M 1972 Superconducting parameters and size effects of aluminum films and foils *Phys. Rev.* B **5** 3558–72
[52] Langley B W, Anlage S M, Pease R F W and Beasley M R 1991 Magnetic penetration depth measurements of superconducting thin films by a microstrip resonator technique *Rev. Sci. Instrum.* **62** 1801–12
[53] Vendik O G, Vendik I B and Kaparkov D I 1998 Empirical model of the microwave properties of high-temperature superconductors *IEEE Trans. Microwave Theory Tech.* **46** 469–78
[54] Javadzadeh S M H, Farzaneh F and Fardmanesh M 2013 Nonlinear circuit model for discontinuity of step in width in superconducting microstrip structures and its impact on nonlinear effects *IEEE Trans. Appl. Supercond.* **23** 1301208